M. Maher, L. Milne, D. de Palacio, K. Redman and C. Roger for recording changeover rates. We also thank D. Bates, P. Harvey, O. Merne and A. Walsh, the Neale family, D. Shaw, M. and L. Smyth, B. Zonfrillo, the Royal Society for the Protection of Birds and the Scottish Seabird Centre for logistical support. S. Bearhop, D. Elston and A. Stien gave statistical advice, while S. Albon, F. Daunt, M. Harris, R. Moss, J. Sherratt and K. Thompson commented on an earlier draft. This project was funded by a Natural Environment Research Council CASE Research Studentship to S.L.

Correspondence and requests for materials should be addressed to T.N.S. (e-mail: T.N.Sherratt@durham.ac.uk) or S.W. (e-mail: swan1@ceh.ac.uk).

Calcitic microlenses as part of the photoreceptor system in brittlestars

Joanna Aizenberg*, Alexei Tkachenko*, Steve Weiner†, Lia Addadi† & Gordon Hendler‡

* *Bell Laboratories/Lucent Technologies, Murray Hill, New Jersey 07974, USA*
† *Department of Structural Biology, The Weizmann Institute of Science, Rehovot 76100, Israel*
‡ *Natural History Museum of Los Angeles County, Los Angeles, California 90007, USA*

Photosensitivity in most echinoderms has been attributed to 'diffuse' dermal receptors[1–3]. Here we report that certain single calcite crystals used by brittlestars for skeletal construction[4,5] are also a component of specialized photosensory organs, conceivably with the function of a compound eye. The analysis of arm ossicles in *Ophiocoma*[6] showed that in light-sensitive species, the periphery of the labyrinthic calcitic skeleton extends into a regular array of spherical microstructures that have a characteristic double-lens design. These structures are absent in light-indifferent species. Photolithographic experiments in which a photoresist film was illuminated through the lens array showed selective exposure of the photoresist under the lens centres. These results provide experimental evidence that the microlenses are optical elements that guide and focus the light inside the tissue. The estimated focal distance (4–7 μm below the lenses) coincides with the location of nerve bundles—the presumed primary photoreceptors. The lens array is designed to minimize spherical aberration and birefringence and to detect light from a particular direction. The optical performance is further optimized by phototropic chromatophores that regulate the dose of illumination reaching the receptors. These structures represent an example of a multifunctional biomaterial that fulfills both mechanical and optical functions.

Echinoderms in general, and especially the brittlestars (Ophiuroidea), exhibit a wide range of responses to light intensity, from a largely light-indifferent behaviour to pronounced colour change and rapid escape behaviour[7]. Figure 1 compares the appearance and the skeletal structure of two species of *Ophiocoma*, which represent the two extreme photosensitivity types. *Ophiocoma pumila* (Fig. 1a) shows no colour change and little reaction to illumination. *Ophiocoma wendtii* is a highly photosensitive species, and it changes colour markedly[7], from homogeneous dark brown during the day (Fig. 1b, left) to banded grey and black at night (Fig. 1b, right). Another conspicuous behavioural response to light is negative phototaxis: *O. wendtii* is able to detect shadows and quickly escape from predators into dark crevices[7], which they are able to identify from several centimetres away[8]. The latter reaction is particularly unexpected in these animals as the behaviour is usually associated with the presence of discrete photosensory organs. No specialized eyes have, however, been documented in brittlestars and their reactions to light have been linked to diffuse dermal receptors[1–3].

The sensitivity to light seems to correlate with the specialized skeletal structure of the dorsal arm plates (DAPs). These ossicles protect the upper part of each joint in brittlestar arms (Fig. 1c). Skeletal elements of echinoderms are each composed of a single crystal of oriented calcite shaped into a unique, three-dimensional mesh (stereom)[4,5,9,10]. The diameter of the typical stereom in the DAPs of *Ophiocoma* is about 10–15 μm (Fig. 1d). In *O. wendtii* as well as in other photosensitive species[6], the outer surface of the DAP stereom bears a characteristic array of enlarged spherical structures 40–50 μm in diameter (Fig. 1d, f). In cross-section they have a remarkably regular double-lens shape (Fig. 1g). The optical axis of the constituent calcite is oriented parallel to the lens axis and perpendicular to the plate surface[9]. The mean geometry of the lenses was inferred from the measurements of lens diameter (L) and thickness (t) in 20 random lenses sectioned through the centre (Fig. 1g):

$$t = 0.89L + 2.2 \quad (1)$$

with a correlation coefficient (r^2) of 0.91. Similar lenses were also

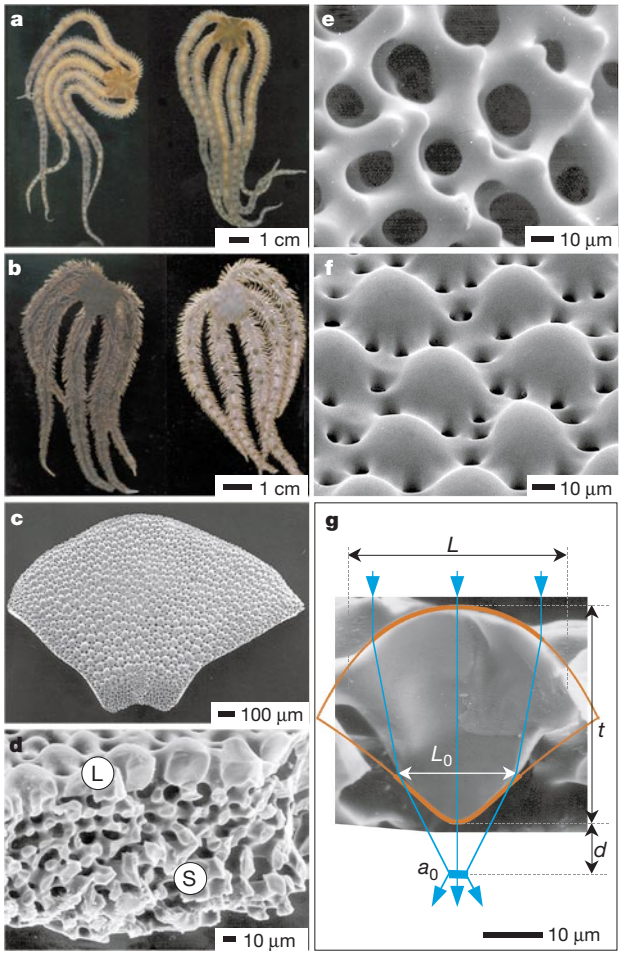

Figure 1 Appearance and skeletal structure of ophiocomid brittlestars. **a**, Light-indifferent species *Ophiocoma pumila* shows no colour change from day (left) to night (right). **b**, Light-sensitive species *O. wendtii* changes colour markedly from day (left) to night (right). **c**, Scanning electron micrograph (SEM) of a dorsal arm plate (DAP) of *O. wendtii* cleansed of organic tissue. **d**, SEM of the cross-section of a fractured DAP from *O. wendtii* showing the typical calcitic stereom (S) and the enlarged lens structures (L) that constitute the peripheral layer. **e**, SEM of the peripheral layer of a DAP of *O. pumila* showing that it lacks the enlarged lens structures. **f**, SEM of the peripheral layer of a DAP from *O. wendtii* with the enlarged lens structures. **g**, High-magnification SEM of the cross-section of an individual lens in *O. wendtii*. Red lines represent the calculated profile of a lens compensated for spherical aberration. The operational part of the calcitic lens (L_0) closely matches the profile of the compensated lens (bold red lines). The light paths are shown in blue.

found on the dorsal region of lateral arm plates. Ventral arm plates and most of the surface of lateral arm plates do not develop enlarged spherical structures, and the orientation of the optical axis of the constituent calcite is not perpendicular to the surface of the plate.

The absence of such structures on the DAPs in various relatively light-insensitive species, such as *O. pumila* (Fig. 1a, e), raises the possibility of the direct involvement of calcitic microlenses in photoreception. Calcitic microlenses were used by the trilobites[11–13]. The presence of transparent regions of compact stereom has been reported also for sea stars[14] and sea urchins[15].We proposed that these calcitic microstructures might have a function in directing and focusing the light on photosensitive tissues.

To detect and visualize the lensing effect, we designed a lithographic experiment (see Fig. 2a). A DAP of *O. wendtii* was cleansed of organic tissue, and a low-magnification scanning electron micrograph (SEM) of its dorsal surface was recorded as a reference image. The inner stereom of the DAP was polished until a 43-μm-thick lens layer, free of the underlying stereom, was produced. This size was chosen to correspond to the thickness of the largest measured lens. The lens layer was placed onto a 5-μm-thick polydimethylsiloxane (PDMS) film and embedded in PDMS. PDMS served two functions: a support and a transparent organic medium with a high refractive index. A film of positive photoresist was spun on a silicon wafer. In preliminary experiments, we studied the depth of the processed photoresist as a function of exposure and set the illumination dose, I_0, just below the sensitivity level of photoresist (Fig. 2b, left). We performed two exposures of photoresist using the lens array embedded in PDMS as a mask[16,17]. In the first experiment, the sample was brought directly into a conformal contact with the photoresist. In the second experiment, an additional 12-μm-thick PDMS film was used between the sample and photoresist. For our fixed exposure conditions (I_0) patterns in the photoresist are recorded only for the regions where $I > I_0$—that is, for the areas exposed with focused light—the size of the spots in the photoresist being equal to the cross-section of the focused beam (Fig. 2b, right).

A comparative analysis of the photoresist surfaces and the reference image of the lens layer made it possible to delineate the region in the lens array (Fig. 2c) and the corresponding patterns in the photoresist obtained at the distances h_1 (48 μm) and h_2 (60 μm) from the upper surface of the lens array, respectively (Fig. 2d, e). Superimposed images of Fig. 2c–e, with the individual lenses outlined, clearly show the selective exposure of photoresist under the lens areas (Fig. 3a). This result unequivocally confirms the focusing ability of the dorsal peripheral layer of the DAP.

Figure 3b presents the rationale for the quantitative analysis of the lensing effect, by describing the focusing action of the lenses located along the dotted line in Fig. 3a. For the family of lenses that produce patterns in both photoresist layers (for example lenses 2 and 4 in Fig. 3b), we can determine distances (x) from the focal point of each

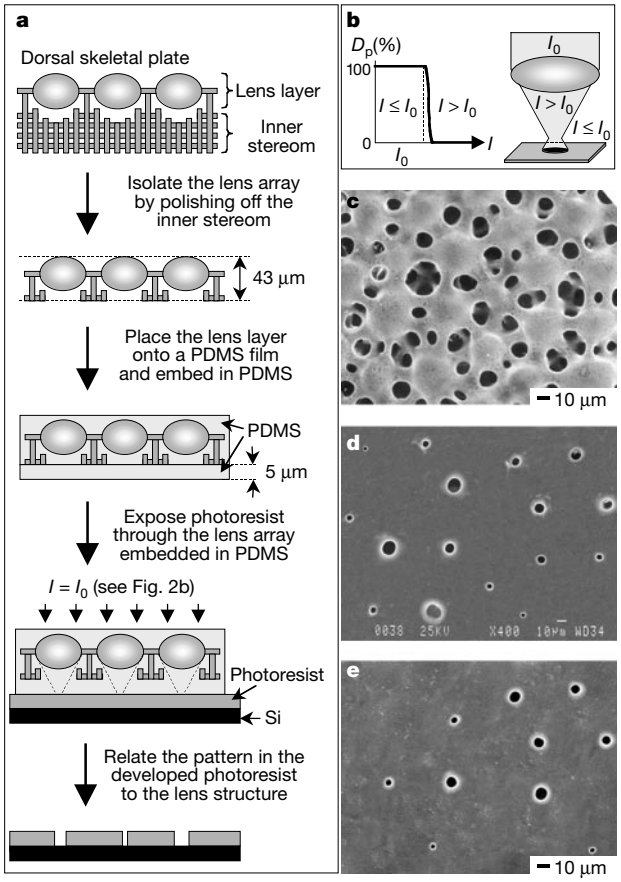

Figure 2 Lithographic experiment showing the focusing ability of the lens layer. **a**, Schematic representation of the experimental procedure (see text for details). **b**, Depth of the processed photoresist layer, D_p, as a function of exposure, I (left). The light intensity for the lithographic imaging of the focusing effect was maintained at the I_0 value, such that only areas exposed with focused light would appear in photoresist (right). **c**, SEM of the analysed area in a lens array of *O. wendtii*. **d, e**, SEMs of photoresist exposed at the distance h_1 (48 μm) (**d**) and h_2 (60 μm) (**e**) from the top surface of the corresponding lens array shown in **c**.

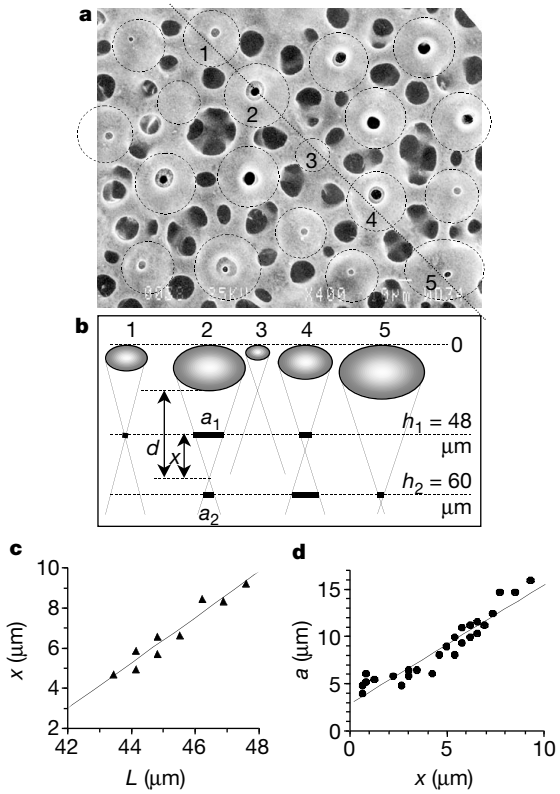

Figure 3 Analysis of the focusing effect of the lens layer. **a**, Superposition of the micrographs shown in Fig. 2c–e. Photoresist is selectively exposed under the lens areas outlined by dashed lines. **b**, Schematic representation of the focusing action of lenses located along the dotted line in **a**. Lenses with a focal plane above h_1 produce narrow features in the first lithographic experiment and no features in the second (lens 1). Lenses with a focal point below h_2 produce narrow features in the second experiment and no features in the first (lens 5). When the focal plane of a lens is located significantly above h_1, no pattern in either photoresist layer is formed (lens 3). Patterns in both photoresist layers are recorded under lenses with a focal point between h_1 and h_2 (lenses 2 and 4). **c**, Distances from the focal points of lenses to the first imaging plane (x) as a function of the lens diameters (L). **d**, Sizes of the spots in photoresist (a) as a function of x.

lens to the first imaging plane:

$$x = a_1(h_2 - h_1)/(a_1 + a_2) \quad (2)$$

where a_1 and a_2 are the measured diameters of the spots recorded at the distances h_1 and h_2 from the top surface of the lens array, respectively. Figure 3c shows that the distances x depend linearly on the lens diameters L:

$$x = 1.14L - 44.8 \quad (3)$$

where r^2 is 0.93.

Equations (1) and (3) allowed us to calculate the experimental position of the focal plane for the lenses operating in PDMS:

$$d = h_1 + x - t \approx 0.25L \approx 6.5\text{–}12.5\ \mu\text{m} \quad (4)$$

Using basic considerations of the geometric optics for a thick lens[18] that has the characteristic shape of the microlenses, we determined the relationship between d and the effective focal length f:

$$f \approx d(1 - (1 - n_1/n_c)t/R_u)^{-1} \approx 1.5d \quad (5)$$

where R_u is the curvature radius of the upper surface of the lens, and n_1 (1.46) and n_c (1.66) are the refractive indices of PDMS and calcite along the c-axis, respectively. The position of the focal point in the actual biological environment, (d_b), can be determined using the thick-lens formula[18] for two media with different refractive indices:

$$d_b \approx d(n_c/n_1 - 1)/(n_c/n_2 - 1) \approx 0.14L \approx 4\text{–}7\ \mu\text{m} \quad (6)$$

where n_2 (1.34) is the refractive index of body fluids[11].

Figure 3d presents the sizes of the spots in the photoresist (a) as a function of x for the entire lens array. Using a linear approximation of the data, $a(x) = 1.26x + 2.9$ ($r^2 = 0.90$), one can estimate the size of the spot at the focal plane, $a_0 = a(x = 0) \approx 2.9\ \mu\text{m}$, and the operational diameter of a typical lens, $L_0 = a(x = f) \approx 20\ \mu\text{m}$. The intensity of the incoming light is thus enhanced at the focal point by a factor of $E = (L_0/a_0)^2 \approx 50$.

For a thick lens formed by two spherical surfaces, a_0 is related to L_0 and f by the equation[18] $a_0 \approx L_0^2/f$. For such a lens, the experimental values of a_0 and f would then correspond to the maximum operational diameter $L_0 \approx 5\text{–}6\ \mu\text{m}$ and the light enhancement factor $E \approx 3\text{–}4$. The experimentally determined values of L_0 and E (see above equations) are significantly higher, clearly indicating that there must exist a marked compensation for spherical aberration[11,12,18]. To verify this conclusion, we calculated the optimal profile for the compensated calcitic lens in a biological medium (red line in Fig. 1g) and found it to be in a good agreement with the actual shape of the operational part of a lens. The proportionality of t and d to L (equations (1), (4) and (6)) suggests that all lenses are rescaled replicas of each other, implying that the entire array is compensated for aberration.

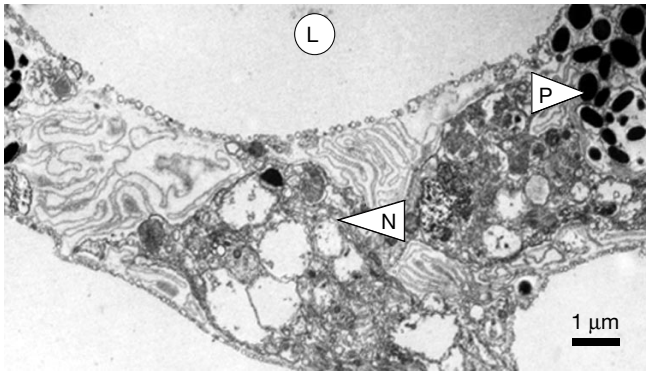

Figure 4 Transmission electron micrograph of the decalcified section of the DAP of *O. wendtii*. Sample preparation is described in ref. 6. L, lens area; N, nerve bundle; P, pigment.

If the calcitic microlenses are involved in photoreception as light guides and concentrators, one should expect the presence of receptors positioned at their focal points. Indeed, a transmission electron microscopy study[6] of thin sections of decalcified DAPs revealed bundles of nerve fibre located at the predicted distance d_b beneath the lens layer (Fig. 4). The diameters of the neural bundles ($b \approx 2\text{–}4\ \mu\text{m}$) correspond well to the estimated size of the focused spot a_0. Furthermore, what is seen as a diurnal colour change of *O. wendtii* (Fig. 1b) is, in fact, a filtering and diaphragm action of chromatophores. These chromatophores regulate the intensity of light reaching the lenses by extending their pigment-filled processes to cover the lens during the day and retracting them to a lateral position between the lenses during the night[6] (Fig. 4). Although the characteristics of echinoderm dermal photoreceptors and their precise locations are poorly understood and controversial[3,6,19,20], the likelihood of sub-lens photoreceptors in *O. wendtii* also corresponds with neurophysiological[21,22] and biochemical[20] data.

On the basis of our results, we suggest that the array of calcitic microlenses with their unique focusing effect and underlying neural receptors may form a specialized photoreceptor system with a conceivable compound-eye capability. For a compound eye to operate, each unit (lens plus photoreceptor) must respond only to light coming from a single direction[23]. The angular selectivity is determined by three principal parameters: first, the angular resolution of the lens, $\phi = a_0/f$. Our experiments yield a ϕ-value of $\sim 10°$. The second parameter is the ratio of the detector diameter to the focal length, m. Although we do not know the effective size of the receptors in *O. wendtii*, we can estimate the maximum value of m that is limited by the diameter of the sub-lensar nerve bundles: $m_{max} = b/f \approx \phi$. The last parameter that determines the angular selectivity is the alignment of the detector with respect to the optical axis. From our observation that the lenses are compensated for aberration, it follows that when light deviates from the optimal direction by ψ, the spot size increases linearly with $|\psi| : a(\psi) - a_0 \approx |\psi|L_0$. This implies that the focal intensity decays as $(|\psi| + \psi^*)^{-2}$, that is, it is sharply peaked in the vicinity of the optimal incident angle, with the characteristic width of the peak ($\psi^* \approx a_0/L_0$) being of the order of the angular resolution ϕ. This effect suggests a plausible mechanism for targeting specific receptors aligned with the lens axis, on the basis of significantly stronger receptor response to the incoming focused light.

The selected nerve bundle will then efficiently detect signals that come only from one direction with the angular selectivity of $\sim 10°$, making the calcitic microlenses suitable for a compound-eye unit. It is doubtful, however, that one DAP could function as a single eye—even though it has a slightly curved shape, the individual lenses are all oriented along the crystallographic c-axis, minimizing the effect of birefringence. This suggests that the entire array is a highly redundant optical element free of aberration that detects the light from a particular direction. As a brittlestar has a large number of DAPs and additional arrays of lenses on the lateral surfaces, all of which are oriented differently and are capable of changing position as the arm moves, it could potentially extract a considerable amount of visual information about its environment. Although we have only limited evidence that the lens apparatus operates at a distance[8], which would conform to the definition of an eye, our results suggest that the presence of such structures may be sufficient to elicit the rapid, coordinated behaviours, such as detection of predators and retreat toward crevices, that imply the occurrence of vision. These are the very abilities that are central to the survival of individuals of *O. wendtii* in their natural habitat[7].

The demonstrated use of calcite by brittlestars, both as an optical element and as a mechanical support, illustrates the remarkable ability of organisms, through the process of evolution, to optimize one material for several functions, and provides new ideas for the fabrication of 'smart' materials[24,25]. □

Received 29 March; accepted 25 June 2001.

1. Hyman, L. H. *The Invertebrates* Vol. 4 (McGraw-Hill, New York, 1955).
2. Millott, N. The photosensitivity of echinoids. *Adv. Mar. Biol.* **13,** 1–52 (1975).
3. Yoshida, M., Takasu, N. & Tamotsu, S. in *Photoreception and Vision in Invertebrates*; (ed. Ali, M. A.) 743–771 (Plenum, New York, 1984).
4. Lowenstam, H. A. & Weiner, S. *On Biomineralization* 123–134 (Oxford Univ. Press, Oxford, 1989).
5. Wainwright, S. A., Biggs, W. D., Currey, J. D. & Gosline, J. M. *Mechanical Design in Organisms* (John Wiley, New York, 1976).
6. Hendler, G. & Byrne, M. Fine structure of the dorsal arm plate of *Ophiocoma wendti* (Echinodermata, Ophiuroidea). *Zoomorphology* **107,** 261–272 (1987).
7. Hendler, G. Brittlestar color-change and phototaxis (Echinodermata: Ophiuroidea: Ophiocomidae). *Mar. Ecol.* **5,** 379–401 (1984).
8. Cowles, R. P. Stimuli produced by light and by contact with solid walls as factors in the behavior of ophiuroids. *J. Exp. Zool.* **9,** 387–416 (1910).
9. Donnay, G. & Pawson, D. L. X-ray diffraction studies of echinoderm plates. *Science* **166,** 1147–1150 (1969).
10. Ameye, L., Hermann, R., Wilt, F. & Dubois, P. Ultrastructural localization of proteins involved in sea urchin biomineralization. *J. Histochem. Cytochem.* **47,** 1189–1200 (1999).
11. Clarkson, E. N. K. & Levi-Setti, R. Trilobite eyes and the optics of Des Cartes and Huygens. *Nature* **254,** 663–667 (1975).
12. Gal, J., Horvath, G., Clarkson, E. N. K. & Haiman, O. Image formation by bifocal lenses in a trilobite eye? *Vision Res.* **40,** 843–853 (2000).
13. Towe, K. M. Trilobite eyes: calcified lenses *in vivo*. *Science* **179,** 1007–1010 (1973).
14. Döderlein, L. Ueber 'Krystallkörper' bei Seesternen. *Denkschr. Med. Nat. Ges. Jena* **8,** 491–494 (1898).
15. Smith, A. B. in *Special Papers in Palaeontology* **25,** 1–81 (Palaeontology Association, London, 1980).
16. Xia, Y. N. & Whitesides, G. M. Soft lithography. *Annu. Rev. Mater. Sci.* **28,** 153–184 (1998).
17. Aizenberg, J., Rogers, J. A., Paul, K. E. & Whitesides, G. M. Imaging the irradiance distribution in the optical near field. *Appl. Phys. Lett.* **71,** 3773–3775 (1997).
18. Flint, H. T. *Geometrical Optics* (Methuen, London, 1936).
19. Cobb, J. L. S. & Moore, A. Comparative studies on receptor structure in the brittlestar *Ophiura ophiura*. *J. Neurocytol.* **15,** 97–108 (1986).
20. Johnsen, S. Identification and localization of a possible rhodopsin in the echinoderms *Asterias forbesi* (Asteroidea) and *Ophioderma brevispinum* (Ophiuroidea). *Biol. Bull.* **193,** 97–105 (1997).
21. Cobb, J. L. S. & Hendler, G. Neurophysiological characterization of the photoreceptor system in brittlestars. *Comp. Biochem. Physiol.* **97A,** 329–333 (1990).
22. Stubbs, T. R. in *Echinoderms* (ed. Lawrence, J. M.) 403–408 (Proc. Int. Echinoderms Conf., Tampa Bay, 1982).
23. Land, M. F. in *Comparative Physiology and Evolution in Invertebrates B: Invertebrate Visual Centers and Behavior I* (ed. Autrum, H.) 471–592 (Springer, Berlin, 1981).
24. Mann, S. & Ozin, G. A. Synthesis of inorganic materials with complex form. *Nature* **382,** 313–318 (1996).
25. Belcher, A. M., Hansma, P. K., Stucky, G. D. & Morse, D. E. First steps in harnessing the potential of biomineralization. *Acta Mater.* **46,** 733–736 (1998).

Acknowledgements

We thank P. Wiltzius and M. Megens for helpful discussions.

Correspondence and requests for materials should be addressed to J.A. (e-mail: jaizenberg@lucent.com).

Delineation of prognostic biomarkers in prostate cancer

Saravana M. Dhanasekaran*, Terrence R. Barrette*, Debashis Ghosh†, Rajal Shah*, Sooryanarayana Varambally*, Kotoku Kurachi‡, Kenneth J. Pienta§‖¶, Mark A. Rubin*§¶# & Arul M. Chinnaiyan*§¶#

*Departments of * Pathology, † Biostatistics, ‡ Human Genetics, § Urology, ‖ Internal Medicine, and ¶ Comprehensive Cancer Center, University of Michigan Medical School, Ann Arbor, Michigan 48109, USA*
 # These authors share senior authorship

Prostate cancer is the most frequently diagnosed cancer in American men[1,2]. Screening for prostate-specific antigen (PSA) has led to earlier detection of prostate cancer[3], but elevated serum PSA levels may be present in non-malignant conditions such as benign prostatic hyperlasia (BPH). Characterization of gene-expression profiles that molecularly distinguish prostatic neoplasms may identify genes involved in prostate carcinogenesis, elucidate clinical biomarkers, and lead to an improved classification of prostate cancer[4–6]. Using microarrays of complementary DNA, we examined gene-expression profiles of more than 50 normal and neoplastic prostate specimens and three common prostate-cancer cell lines. Signature expression profiles of normal adjacent prostate (NAP), BPH, localized prostate cancer, and metastatic, hormone-refractory prostate cancer were determined. Here we establish many associations between genes and prostate cancer. We assessed two of these genes—hepsin, a transmembrane serine protease, and pim-1, a serine/threonine kinase—at the protein level using tissue microarrays consisting of over 700 clinically stratified prostate-cancer specimens. Expression of hepsin and pim-1 proteins was significantly correlated with measures of clinical outcome. Thus, the integration of cDNA microarray, high-density tissue microarray, and linked clinical and pathology data is a powerful approach to molecular profiling of human cancer.

We developed a 9,984-element (10K) human cDNA microarray to analyse gene expression profiles in benign and malignant prostate tissue. As with previous cancer profiling studies[7–10], molecular classification of prostate cancer was one of the goals of this analysis. We used two distinct reference samples for comparative microarray analysis: NAP tissue from patients with prostate cancer, and prostate tissue from men without documented prostate pathology. By making direct comparisons against normal tissue counterparts, we took advantage of a 'subtractive' effect, which emphasized genes that consistently distinguished normal and neoplastic tissues.

Prostate tissues used in microarray analysis included 4 BPH samples, 8 NAP samples, 1 commercial pool of normal prostate tissue (from 19 individuals), 1 prostatitis sample, and 11 localized and 7 metastatic prostate-cancer samples. Three cell lines from metastatic prostate cancer (DU-145, LnCAP and PC3) were also profiled for gene expression. Twenty-eight additional prostate tissue specimens were profiled and the data included in the Supplementary Information (samples of 9 BPH, 1 NAP, 13 metastatic and 5 localized prostate cancers). Fluorescently labelled (Cy5) cDNA was prepared from total RNA from each experimental sample. A second distinguishable fluorescent dye (Cy3) was used to label the two reference samples used in this study: a pool of NAP from four independent patients with prostate cancer and a commercial pool of normal prostate tissues. A direct comparison between the NAP and commercial pools was also made and notable differences in gene expression were readily apparent (Fig. 1 and Supplementary Information).

In all, more than 80 cDNA microarrays were used to assess gene expression in four clinical states of prostate-derived tissues and two distinct reference pools of normal specimens. Figure 1 provides an overview of the variation in gene expression across the different tissue specimens analysed (the full data set and 28 further samples can be seen in the Supplementary Information). A hierarchical clustering algorithm was used to group genes and experimental samples on the basis of similarities of gene expression over all that were tested. Relationships between the experimental samples are summarized as dendrograms (Fig. 1a), in which the pattern and length of the branches reflect the relatedness of the samples. Benign conditions of the prostate, such as BPH and NAP, cluster separately from malignant prostate-cancer cell lines or tissues, regardless of the reference pool used. Within the prostate-cancer cluster, metastatic and clinically localized prostate cancer formed distinct subgroups.

Eisen matrix formats[11] of the variation in gene expression show clusters of coordinately expressed genes, highlighting relationships between specimens (black bars in Fig. 1b, c). For example, clusters B3 and C1 represent genes downregulated in both localized and metastatic prostate cancer (Fig. 1b, c). By contrast, clusters B6 and B4 highlight genes that are specifically up- or downregulated in metastatic prostate cancer, respectively (Fig. 1b). *IGFBP-5*, *DAN1*, *FAT* tumour suppressor and *RAB5A* are examples of genes that are downregulated specifically in metastatic prostate cancer and also have a proposed role in oncogenesis (magnified regions, Fig. 1b).